Scientific Research

Experimental Study on the Shear Capacity of Hollow Core Slabs with End-regional Oblique Cracks

Jie Li

Shanghai Municipal Road Transport Development Center, Shanghai 200001, China.
* Correspondence: 553766202@qq.com

Abstract: This paper presents an experimental investigation into the shear capacity of prestressed concrete (PC) hollow core slabs with and without pre-existing oblique crack damage. A salvaged hollow core slab from Taihe Road Viaduct was selected for testing, with one end exhibiting in-service crack damage (T-A side) and the other end remaining intact (T-B side). Both ends were subjected to static loading to failure, and their shear performance was compared. The results indicate that the ultimate shear capacity of the damaged T-A side was approximately 16% lower than that of the undamaged T-B side. The damaged end also exhibited a lower cracking load, greater ultimate deflection, and greater torsional deformation. Both ends failed in a "bond-shear" mode, but the presence of pre-existing cracks on the T-A side exacerbated crack propagation and led to a wider main failure crack. The experimental results were used to evaluate the accuracy and applicability of several shear capacity calculation methods, including JTG 3362—2018, AASHTO LRFD Specifications 2020, ROSS, Naji, and Zhang's models, and the Response2000 program. The comparison reveals that Zhang's model and the ROSS model provided the most accurate predictions relative to the experimental values. The AASHTO LRFD method was found to be slightly unconservative for the damaged side (V_t/V_{pre} = 0.94) while providing a conservative prediction for the undamaged side. This study highlights the detrimental effects of in-service cracks and reveals limitations in some conventional codes for assessing damaged members.

Keywords: hollow core slab; oblique cracks; end region damage; shear bearing capacity; experimental study; design codes

Citation: Li, J. Experimental Study on the Shear Capacity of Hollow Core Slabs with End-regional Oblique Cracks. *Prestress Technology* **2025**, *3*, 23-37. https://doi.org/10.59238/j.pt.2025.03.002

Received: 04/08/2025
Accepted: 26/08/2025
Published: 30/08/2025

Publisher's Note: Prestress technology stays neutral with regard to jurisdictional claims in published maps and institutional affiliations.

1 Introduction

Prestressed concrete (PC) bridges are important part of modern infrastructure because of their efficient construction and cost effectiveness. However, because they are designed for long-term use, understanding their structural behavior, especially the defects that may occur during operation is critical [1–3]. While longitudinal cracks can form during construction because of prestress transfer, this study focuses on diagonal cracks that appear at the ends of PC hollow core slabs while the bridge is in service [4]. These cracks may be caused by factors such as vehicle overloading, localized stress concentrations from bearing detachment, or gradual damage from hinge joint deterioration [5–7].

Cracks in critical end regions of PC hollow core slabs can severely weaken their structural performance [8–10]. These cracks may reduce shear capacity, alter load transfer mechanisms, and potentially lead to issues such as progressive debonding of prestressing strands or concrete spalling. Murray et al. [11] investigated 45-year-old AASHTO Type II girders with corrosion damage at the ends and reported that corrosion-induced cracks and concrete spalling affected the shear capacity and strand bonding observed during their service time. Similarly, Ross et al. [12] inspected 30-year-old AASHTO Type III girders and observed minor cracks and efflorescence, although these were not considered critical initially. Ross et al. [3] also reported that certain bearing pad designs could cause torsional movement, leading

to deck cracking near panel joints. Such issues can worsen existing cracks or create new ones, highlighting the need for further research.

Research has shown that shear cracks near supports can disrupt strand anchorage, leading to bond loss and strand slippage and reducing both shear strength and flexural strength. While these failures are usually observed at almost the ultimate load during laboratory tests, underlying cracking mechanisms can be triggered by operational stress. Zhang et al. [5] confirmed that strand debonding significantly weakens the shear strength of PC hollow slabs and reported that this debonding induced bond-loss failure prevents strength improvement even with increased concrete compression zone strength. Tawadrous and Morcous [13]also explored the shear strength of deep hollow slabs, finding inconsistencies in various code predictions and the crucial role of the bearing support length on the shear capacity. However, a specific understanding of how oblique cracks affect the shear performance of PC hollow core slabs remains limited.

To address these limitations, this study presents an experimental and analytical investigation into the effect of operational oblique cracks on the shear-bearing capacity of PC hollow core slabs. The objectives of this study are threefold: to experimentally compare the shear performance of a damaged beam end against that of an intact beam under eccentric loading; to evaluate the accuracy and conservatism of several conventional design codes (JTG 3362—2018 [14], AASHTO LRFD Specifications [15]) and advanced theoretical models (including those by ROSS [16], Naji [10], Zhang [5], and the Response2000 program [17]); and to provide a critical reference for the in-service safety evaluation of similar hollow core slab beams. These findings are intended to inform future maintenance and assessment strategies for aging PC bridge infrastructure.

2 Engineering Background

The Taihe Road Viaduct is situated in the northwest section of Shanghai's Outer Ring Expressway (S20) and was completed and opened to traffic in 2001. The bridge is divided into two segments. Its standard width is 17 m and is arranged as 0.5 m (barrier) + 16 m (carriageway) + 0.5 m (barrier), totaling 17 m. The bridge deck has an asphalt concrete pavement layer. The bridge was designed to accommodate heavy vehicle loads, including Automobile-Super 20 and Trailer-120, and was subjected to a special 300t load verification. The superstructure of the bridge incorporates PC hollow core slab beams with spans ranging from 11.5 m to 30 m. The substructure consists of pile–column piers and abutments, utilizing spherical crown-type rubber bearings.

The bridge's technical condition was evaluated in accordance with the "Technical Condition Evaluation Standard for Highway Bridges" (JTG/TH21—2011). By employing a layered comprehensive evaluation methodology combined with five categories of single control indicators, the left segment of the bridge was classified as a Class 3 bridge, indicating "moderate defects, yet capable of maintaining normal service function". Technical condition of the bridge progressively deteriorated annually, marked by the consistent emergence of new defects. Consequently, the bridge was slated for complete superstructure demolition and reconstruction in 2024.

To investigate the influence of damage on the behavior of the hollow core slab, a specific beam (left segment, slab 76-11#, a middle unit) characterized by crack damage at one end and an undamaged state at the other was selected for comparative analysis. The structural configuration of this selected slab is shown in Figure 1. The hollow core slab is 21.12 m in length, 0.9 m in height, and 0.99 m in width. The pretensioned steel strands consist of high-strength, low-relaxation strands with a diameter of 15.24 mm, conforming to the "Steel Strand for Prestressed Concrete" (GB/T 5224—1995) standard. Each strand possesses a nominal cross-sectional area of

 https://doi.org/10.59238/j.pt.2025.03.002

140 mm², a specified standard strength of 1,860 MPa, and a controlled tensioning stress of 1,295 MPa. The slab incorporates six distinct debonding lengths for the pretensioned strands, as detailed in Table 1. A minimum concrete cover of 40 mm is maintained for the prestressing strands.

Surface crack inspection of the hollow core slabs revealed the following characteristics at the end adjacent to Pier T-B (Pier 76#): cracking extended over a range of 1.75 m. The left web exhibited a single longitudinal crack measuring 0.06 mm in width. The right web presented four oblique cracks and two longitudinal cracks, with a width of 0.55 mm. The soffit of the beam displayed two oblique cracks, two transverse cracks, and two longitudinal cracks. A network of cracks was present in the previously repaired region, with the maximum crack width reaching 0.65 mm after surface preparation. The distribution of these pathological cracks at the damaged end is illustrated in Figure 2. Rebound hammer tests were conducted on six selected test zones on the slab's web, yielding the concrete strength results presented in Table 2.

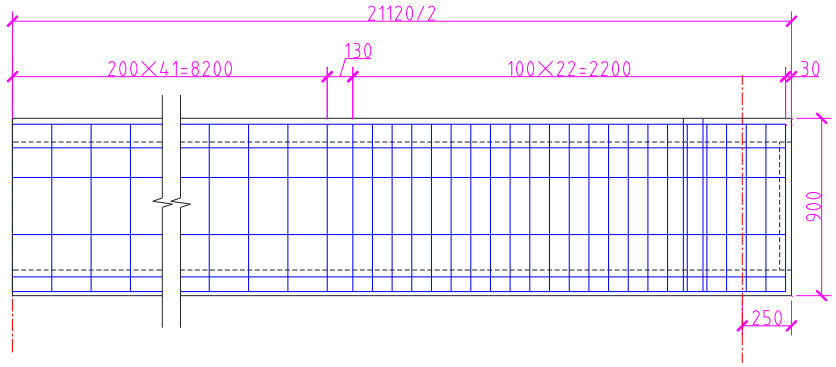

a) Elevational review

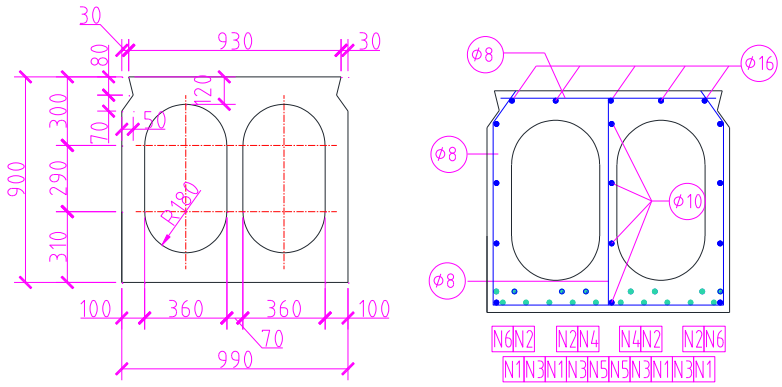

b) Sectional dimensions

Figure 1 Construction details of the hollow core slab

Table 1 Pretensioned strand debonding length

Strand No.	Debonding Length /m	Number of Strands
N1	0	4
N2	1	4
N3	2	4
N4	3	2
N5	4	2
N6	5	2

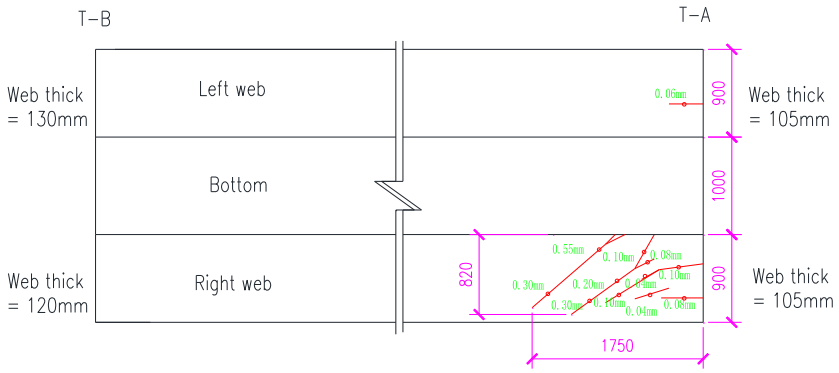

Figure 2 Distribution of pathological cracks at the damaged end

Table 2 Concrete rebound test results

Slab No.	Rebound Mean Value /MPa						Strength Conclusion /MPa
	1	2	3	4	5	6	
76-11#	58.9	58.1	58.5	56.2	54.8	53.3	>60.0

3 Experimental Design

3.1 Experimental Parameters

The primary objective of this experiment is to conduct a detailed comparative analysis of the shear performance between hollow core slabs with existing damage and those in an undamaged state. The design parameters for the test beams are summarized in Table 3. Considering the T-A (Pier 75#) beam end, which displays a crack distribution extending 1.75 m, the loading point was set at a distance-1.75 m from the beam end. With the support positioned 0.25 m from the beam end, the shear span length was established as 1.5 m. Given an effective depth of 0.86 m, the calculated shear span-to-depth ratio (a/d) for the loading configuration is 1.74.

To simulate adverse conditions related to hinge joint failure, specifically addressing the eccentric application of wheel loads on hollow core slabs, the side with more web cracks was chosen as the eccentric loading side. This setup aimed to replicate the maximum eccentricity of wheel loads on a single slab, accounting for a 45-degree load diffusion angle from the bridge deck pavement to the top of the beam. Consequently, the determined load eccentricity from the centerline of the hollow core slab's centerline is 0.215 m.

Table 3 Design Parameters

No.	Damage State	Beam End Crack Range /m	Support Distance from Beam End /m	Shear Span Length /m	Shear Span Ratio	Eccentricity /m
T-A	Damaged	1.75	0.25	1.5	1.74	0.215
T-B	Undamaged	/	0.25	1.5	1.74	0.215

The experimental loading conditions were designed based on the engineering background requirements. Using Bridge Doctor software and in accordance with the "General Specifications for Design of Highway Bridges and Culverts" (JTG D60—2015), the design load combinations for the loading section were calculated. The load values for the frequent, standard, and basic combinations were obtained, as presented in Table 4.

https://doi.org/10.59238/j.pt.2025.03.002

Table 4 Design Shear Combinations for the Loading Section

Loading Section Distance from Support /m	Frequent Combination /kN	Standard Combination /kN	Basic Combination /kN
1.5	287.25	382.75	553.05

3.2 Loading Setup and Procedure

The hollow core slab is quite long, so the loading test was carried out at an outdoor laboratory located in Shanghai. The loading setup is shown in Figure 3. Each end of the beam was fitted with two plate-type rubber bearings, matching the conditions of the actual bridge. Vertical loads were applied using 200-ton hydraulic jacks, and the load magnitude was measured by load sensors. The loading reaction system consisted of a ground anchor beam, anchor rods, and steel crossbeams.

The static loading failure test was first conducted on the T-A side, followed by the static loading failure test on the T-B side. Even after the T-A side experienced shear failure, its remaining shear strength was sufficient to withstand the reaction forces generated by the loading of the T-B side because of the relatively small shear span ratios on both sides of the test beam.

Before the loading test began, the connection reliability and safety of the loading system were checked. Data from the concrete strain gauges, displacement sensors, and pressure sensor channels were monitored to ensure stability. The loading procedure was as follows:

(1) A 50 kN pre-load was applied to the slab three times to check the system function and eliminate non-elastic deformation. The sensors were then zeroed.
(2) Stepped loading in 50 kN increments began, up to the standard load combination for crack resistance.
(3) Loading continued in 50 kN increments to the basic load combination for the bearing capacity.
(4) Loading proceeded in 50 kN increments until beam failure.

Figure 3 On-site loading diagram

3.3 Measurement Layout

The experimental measurements included load, concrete strain, prestressed strand slip, displacement, and crack width. Load cells were installed at the bottom of

the hydraulic jacks to measure the applied load, serving as a reference for graded loading magnitudes.

Displacement sensors were positioned at the support sections, loading sections, and midspan sections. To account for section torsion caused by eccentric loading, two displacement sensors were placed at each measurement section, 50 mm from the beam's edge lines.

Concrete strain measurements included the top normal strain, bottom normal strain, web normal strain, and web principal strain. The layout of the concrete strain measurement is shown in Figure 4. In the concrete strain gauge numbering, "B" indicates the bottom strain, "U" indicates the top strain, and "C" indicates the web strain. The second letter in the concrete strain gauge numbering, "L", denotes the T-A side, whereas "R" denotes the T-B side.

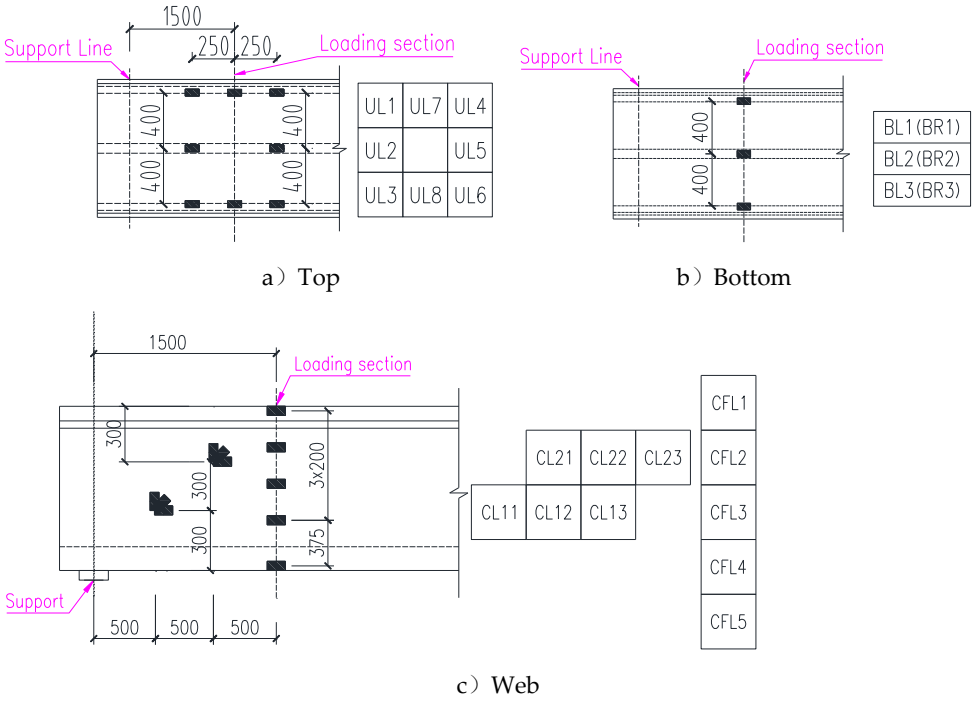

Figure 4 Concrete strain gauge layout and numbering

To monitor the bond-slip amount of the steel strands during the test, plunger-type displacement sensors were used. Before installation, the concrete cover at the end of the hollow core slab was ground down to expose the strand ends. Further, the base of the displacement sensor was fixed to the beam end, and its plunger tip was pressed against the strand end to measure the relative slip between the strand and the concrete. The layout and numbering of the strand slip measurements are shown in Figure 5.

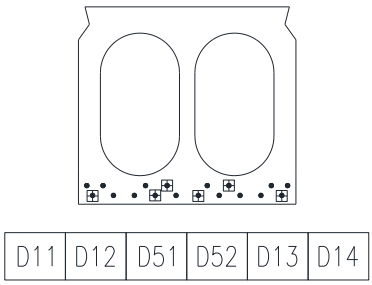

Figure 5 Strand slip measurement layout and numbering

https://doi.org/10.59238/j.pt.2025.03.002

4 Experimental Results and Analysis

4.1 Comparison of Crack Development

Crack development on the T-A side, which had pre-existing damage, can be compared with that on the T-B side, which was initially undamaged. On the T-A side, the right web had two large initial oblique cracks. Crack I, located approximately 300 mm from the support, extended from the bottom to the top and had an initial width of 0.36 mm; however, this crack did not develop into the main failure crack. The second crack, Crack II, was located approximately 900 mm from the support, extended from the bottom to the top and had an initial width of 0.53 mm.

The crack distributions for the T-A side and T-B side are shown in Figures 6 and 7, respectively. As the load increased, the width of the initial oblique cracks I and II on the T-A side of the right web remained largely unchanged, as shown in Figure 8. On both sides, new cracks and significant crack development began at a similar load level of approximately 400 kN. During the loading process, Crack II continued to grow and eventually became the main failure crack, which developed from a crack already present at a width of 0.53 mm into the primary failure crack with a final width of 1.7 mm. On the T-B side, the main failure crack was a new crack that initiated and rapidly grew at a distance of approximately 700 mm from the support, reaching a width of 1.2 mm.

Crack development on the T-A side was more severe. The width of the main failure crack reached 1.7 mm, which was significantly greater than the maximum crack width of 1.2 mm observed on the T-B side. This finding indicates that the presence of pre-existing oblique crack damage at the T-A beam end had negative affect on crack development under loading. The failure of the damaged end was a continuation and exacerbation of an existing defect, leading to a much wider and more severe final crack state than that of the initially undamaged T-B side. These results indicate that initial damage combined with eccentric loading can intensify crack behavior and potentially weaken the shear performance of a beam.

a) Right web b) Left web

Figure 6 Crack distribution for the T-A side

a) Right web b) Left web

Figure 7 Crack distribution for the T-B side

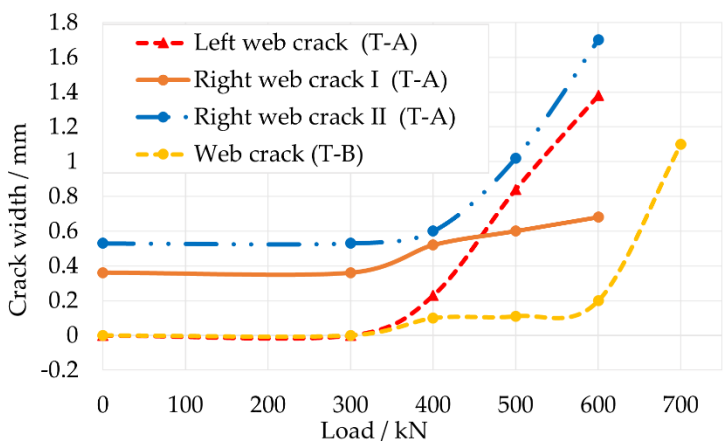

Figure 8 Crack width development

4.2 Load–Displacement and Torsional Angel Curves

In the subsequent analysis, owing to the three-point asymmetric loading configuration used for the test beam, all the loads are represented by the shear load at the cross-section to better describe the load–deformation characteristics. The load–displacement curve for the T-A side (Figure 9) shows that the slab exhibits initial linear-elastic behavior up to a shear load of approximately 340 kN. Beyond this point, the curves for both the left and right webs become non-linear, indicating a reduction in stiffness due to cracking. The right web curve displays a significant decrease in load-carrying capacity after reaching its peak, followed by a post-failure segment. The ultimate load for both webs is 741.3 kN, with the right web reaching a maximum displacement of 18.03 mm, which is notably greater than the 16.28 mm displacement of the left web. The load–torsional angle curve for the T-A side shows a non-linear increase in the torsional angle after the 300 kN load level. The maximum torsional angle recorded is 0.4° at the peak shear load.

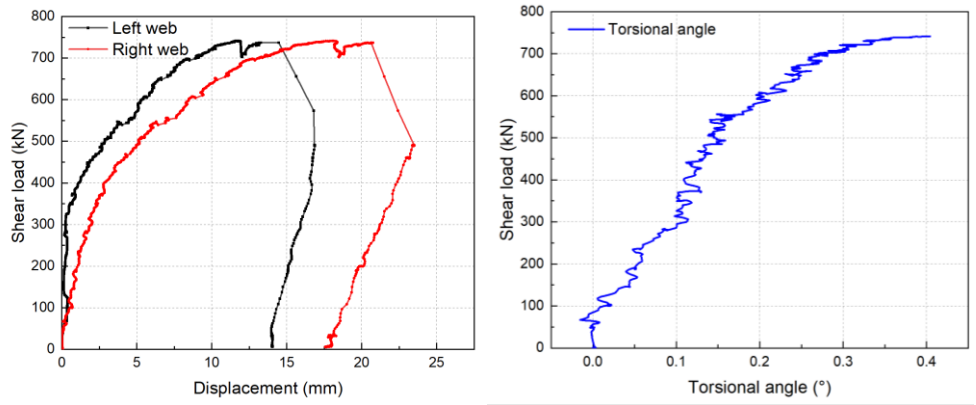

a) Displacement b) Torsional angle

Figure 9 Load–deformation curves for the T-A side

In comparison, the load–displacement curve for the T-B side (Figure 10) demonstrates a significantly stiffer response than that for the T-A side. The initial linear-elastic phase extends to a higher load of approximately 460 kN. Compared with the T-A side, the ultimate shear load reaches 921.3 kN, which is a substantial increase. The maximum displacement at failure is 13.18 mm for the right web, which is less than that observed for the T-A side. The load–torsional angle curve for the T-B side is nearly linear throughout the loading process. Additionally, during continuous data acquisition for the T-B side, an error occurred in the deflection measurement for the left web. As a result, only partial data for the torsional angle is

 https://doi.org/10.59238/j.pt.2025.03.002

valid. The maximum torsional angle recorded at a load of approximately 700 kN is only approximately 0.1°, indicating that compared with the T-A side, the T-A side experiences much less torsional deformation.

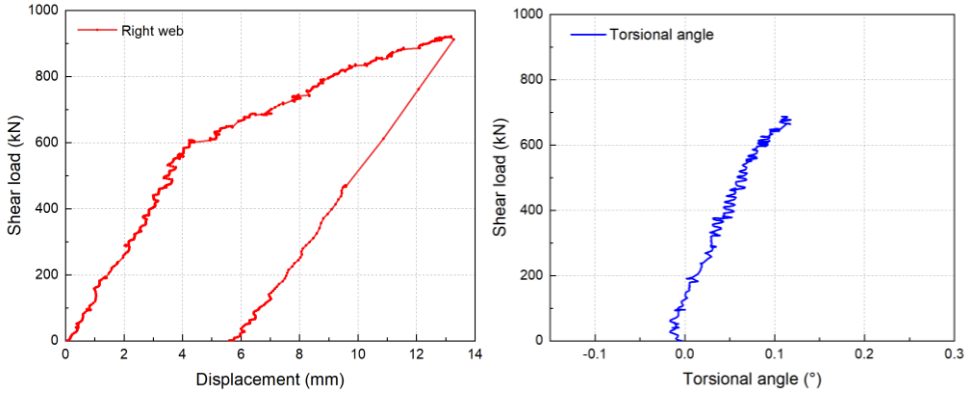

a) Displacement b) Torsional angle

Figure 10 Load-deformation curves for the T-B side

In summary, the damaged T-A side exhibited a weaker and more flexible response, reaching a lower ultimate load with significantly greater torsional deformation and a notable decrease in load-carrying capacity after its peak. In contrast, the undamaged T-B side demonstrated more robust and stiff behavior, achieving a higher ultimate load with a more controlled deformation pattern and substantially less torsion. This finding indicates a clear negative effect of the initial damage on the overall shear performance of the beam.

4.3 Strand slip

Based on the strand slip curves (Figure 11), a clear difference in behavior is observed between the two beam ends. On the T-A side, strand slip initiates at a relatively low load, with the amount of slip increasing significantly and nonlinearly as the shear load increases. The ultimate slip displacement for some strands (e.g., D51 and D52) is very large, exceeding 10 mm at the ultimate shear load of 741.3 kN, indicating a progressive and extensive loss of bond.

In contrast, the T-B side exhibits much less strand slip overall. Slip remains minimal and controlled until a high shear load of approximately 600 kN is reached. Even at a maximum load greater than 900 kN, the maximum recorded strand slip is only approximately 3.5 mm. This demonstrates a more effective strand–concrete bond on the undamaged side, allowing the beam to sustain a much greater load with significantly less slip displacement.

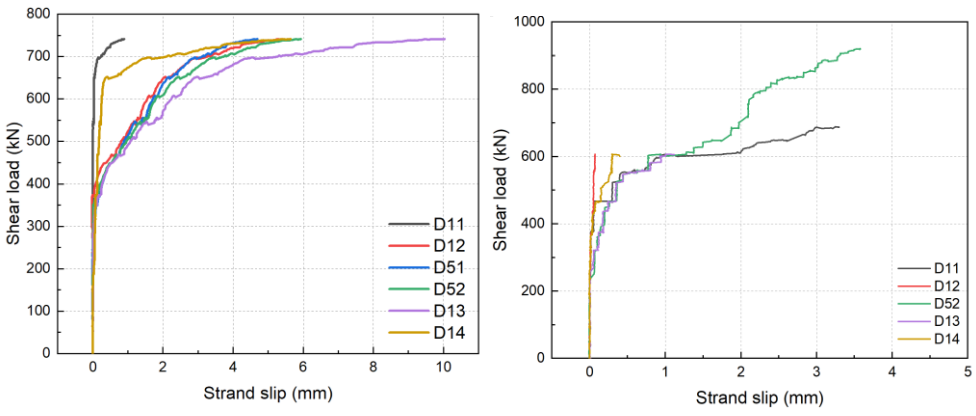

a) T-A side b) T-B side

Figure 11 Strand slip

4.4 Concrete strain

For the T-A side (Figure 12), the compressive strain of the top flange concrete steadily increased until approximately 400–500 kN, after which the rate of strain increased nonlinearly. At the ultimate load, the compressive strains ranged from approximately -300 to -600 με. The tensile strains of the bottom flange concrete increased linearly to approximately 300 kN, with one gauge (BR2) recording a maximum tensile strain of approximately 950 με, which is indicative of significant cracking in the tension zone.

On the T-B side (Figure 13), the top flange concrete exhibited a linear-elastic response up to a load of approximately 600 kN, with a higher ultimate load capacity. The maximum compressive strains were substantial, with some gauges (UL1 and UL2) exceeding -1000 με, suggesting crushing of the concrete at failure. The bottom flange concrete experienced tensile strains that were generally lower than those of the T-A side, reaching a maximum of approximately 500 με.

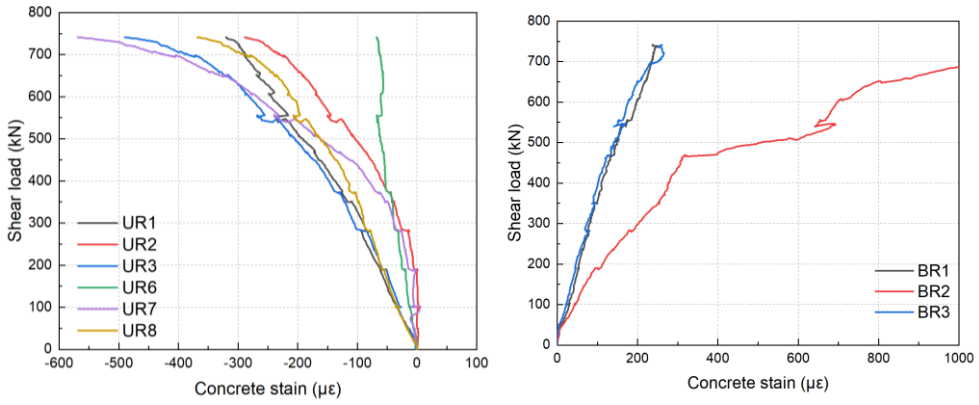

a) top b) bottom

Figure 12 Concrete strain for the T-A side

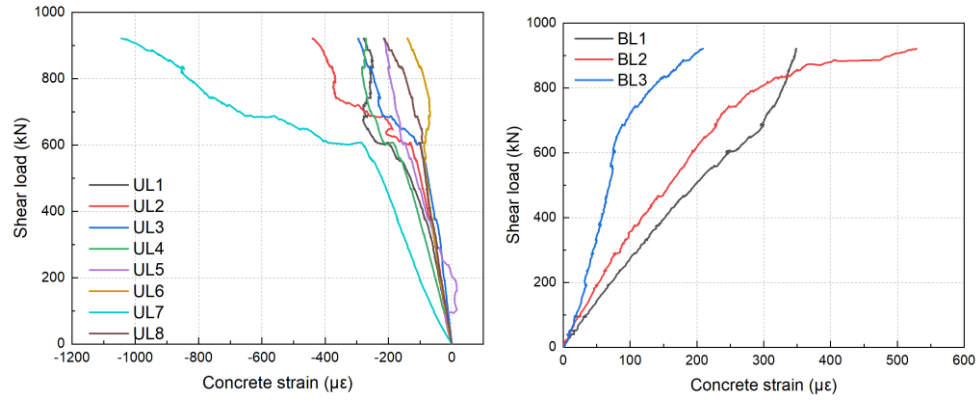

a) top b) bottom

Figure 13 Concrete strain for the T-B side

5 Discussion

5.1 Comparison and Verification of Shear Performance

The experimental shear performance characteristics of the hollow core slabs are summarized in Table 5. The ultimate shear force is defined as the sum of the applied shear load and the self-weight effect of 289.24 kN. This distinction provides a clearer understanding of the load-carrying capacity of the test samples. The ultimate shear force for the T-B side, at 1,065.92 kN, is significantly greater than that of the T-A side,

https://doi.org/10.59238/j.pt.2025.03.002

which is 885.92 kN. This represents a decrease in the ultimate shear capacity of approximately 16% for the damaged T-A side.

In terms of deformation characteristics, the T-A side exhibited an ultimate deflection of 18.03 mm, which is greater than the 13.18 mm recorded for the T-B side. A greater difference is observed in torsional behavior, where the T-A side reaches a maximum torsional angle of 0.40°, which is substantially greater than the measured on the T-B side. This finding indicates that the initial damage on the T-A side resulted in a less stiff and less stable response under eccentric loading.

Finally, when the ultimate shear capacity was compared against the design basic load combination of 540.0 kN, the safety margin of the T-B side was 1.96 greater than that of the T-A side (1.63). This analysis confirms that the pre-existing damage on the T-A side negatively affected its cracking resistance, load-carrying capacity, and overall structural stability, thereby reducing its safety margin.

Table 5 Summary of the Experimental Results

No.	Ultimate Shear /kN	Ultimate Displacement /mm	Max. Torsional Angle /°	Cracking Load /kN	Basic Combination /kN	Safety Margin
T-A	885.92	18.03	0.40	340	540.0	1.63
T-B	1,065.92	13.18	0.25	460	540.0	1.96

5.2 Failure Mode Determination

The failure modes observed in the experiments were characterized by referencing a model proposed by Naji and Ross [16]. This model, illustrated in Figure 14, provides a framework for classifying bond-loss failures based on typical crack patterns and structural behavior. The bond-shear failure mode begins with the formation of inclined cracks in the web and bottom flange near the girder end. These cracks disturb the anchorage of the prestressing strands, which leads to a loss of the strand–concrete bond and slipping of the strands relative to the concrete. The peak load is limited by the reduced tensile force resulting from the loss of bond, which ultimately leads to shear failure. Unlike other failure modes, the concrete in the compression zone does not experience bond-shear failure.

On the T-A side, the main oblique failure crack was located approximately 900 mm from the support. Strand slip, a key indicator of bond loss, initiated at 48% of the ultimate load (Figure 15 a)). This behavior is classified as “bond-shear failure”, where bond loss precedes and leads to shear failure.

The main oblique failure crack on the T-B side was located approximately 700 mm from the support. Strand slip began at a lower percentage of the ultimate load, specifically 35%. Despite this difference in the trigger point, the failure mode is also classified as “bond-shear failure”, which is consistent with the observed mechanics of crack development and subsequent strand slip.

Both the damaged T-A side and the undamaged T-B side ultimately failed in the same “bond–shear failure” mode. This mode is consistent with the general behavior of girders subjected to shear with a small shear span-to-depth ratio. However, distinct differences in failure progression were observed. The initiation of strand slip occurred at different load percentages relative to the ultimate capacity for each side. Furthermore, the location of the main oblique crack varied between the two ends, appearing closer to the support on the undamaged T-B side. This suggests that while the fundamental failure mode was consistent, the pre-existing damage on the T-A side likely influenced the location and progression of the failure, even if the overall classification remained the same.

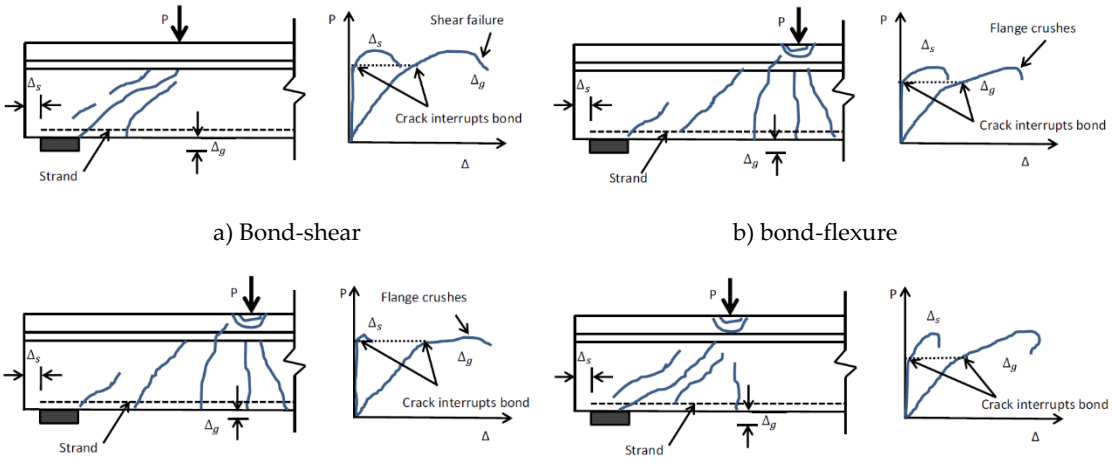

a) Bond-shear b) bond-flexure

c) flexure-bond d) bond-shear/flexure

Figure 14 Typical crack pattern and structural behavior [16]

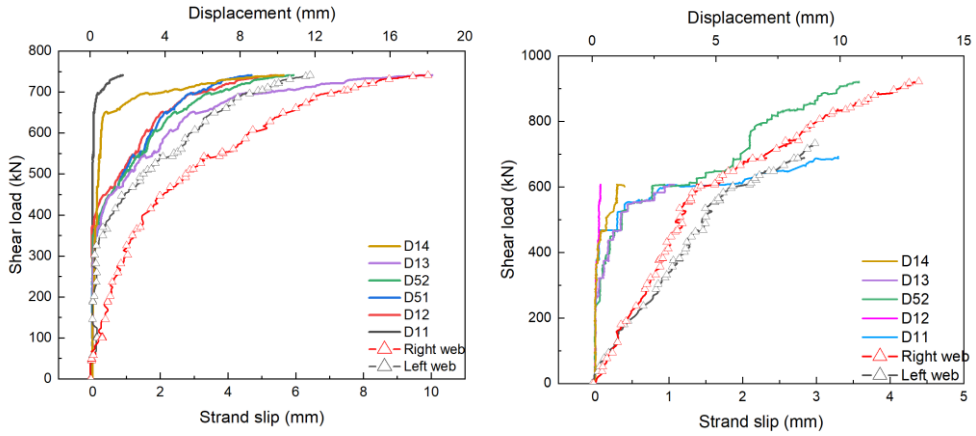

a) T-A b) T-B

Figure 15 Comparison of strand slip and displacement

5.3 Comparison of Experimental Results with Various Calculation Methods

In this section, the experimental shear capacities of the hollow core slabs are compared with predictions from several theoretical models and design specifications, including JTG 3362—2018 [14], AASHTO LRFD Specifications 2020 [15], methods by ROSS [9] and Naji [10], Zhang's refined method [5], and the Response2000 program [17].

The ROSS and Naji models are centered on the transmission of shear in the end region and a bond-loss failure mode due to strand slip from cracks. They operate on the principle that shear cracks cause a loss of strand anchorage, leading to a loss of bond and strand slip. While both models use similar formulas, the key difference lies in how they account for the shear strength provided by the stirrups: ROSS relies on an empirical formula, whereas Naji employs an optimized method based on the least squares technique, . Both models assume that the main failure crack extends directly from the loading point to the edge of the near support.

Zhang's model was developed to address a significant discrepancy in the crack pattern assumption used by the ROSS and Naji models. Experimental results, particularly for Chinese PC hollow core slabs, revealed that failure cracks do not always form at the support edge. Therefore, Zhang's refined model accounts for four key factors: (i) a more realistic oblique crack angle (θ), (ii) the depth of the uncracked

 https://doi.org/10.59238/j.pt.2025.03.002

concrete (ξ_d), (iii) the dowel action provided by longitudinal reinforcement (V_d), and (iv) the specific anchorage length of the pre-stressing strands.

The Response2000 Program is a non-linear sectional analysis program developed at the University of Toronto. It is used to analyze the shear behavior of reinforced concrete members on the basis of the principles of modified compression field theory (MCFT).

JTG 3362—2018 and AASHTO LRFD 2020 are general design specifications used as a baseline for comparison. JTG 3362 considers the combined contribution of concrete and stirrups to shear resistance, whereas AASHTO LRFD provides separate calculations for these components.

The comparative analysis is based on the ratio of the experimental-to-predicted shear capacity (V_t/V_{pre}), as shown in Table 6. A ratio greater than 1 indicates a conservative prediction, whereas a ratio less than 1 suggests an unconservative prediction.

Table 6 Ratio of Experimental-to-Predicted Shear Capacity

No.	JTG—3362	AASHTO	ROSS	Naji	Zhang	Response 2000
T-A	1.10	0.94	1.02	1.74	1.08	1.17
T-B	1.79	1.13	1.23	2.09	1.18	1.41

The analysis of these ratios reveals several key findings. Zhang's model (1.08 for T-A and 1.18 for T-B) and the ROSS model (1.02 for T-A and 1.23 for T-B) demonstrate the highest accuracy, with their predictions closely matching the experimental values. Naji's model is the most conservative, consistently providing the largest safety margins (1.74 and 2.09), which can be attributed to its refined and cautious approach. Notably, the prediction of the AASHTO LRFD method for the damaged T-A side (0.94) is slightly unconservative, whereas its prediction for the undamaged T-B side (1.13) is conservative. These findings highlight the potential limitations of the AASHTO model in accurately assessing the capacity of beams with preexisting damage.

6 Conclusion

This study presents an experimental and analytical investigation into the shear performance of PC hollow core slabs with and without pre-existing oblique crack damage. A salvaged slab from the Taihe Road Viaduct was tested to compare the shear behavior of a damaged end against that of an undamaged end under eccentric loading. The key findings from this research are as follows:

(1) Compared with the undamaged T-B side, the damaged T-A side exhibited significant degradation in shear performance. The ultimate shear capacity of the damaged end was approximately 16% lower. It also demonstrated a lower cracking load (340 kN vs. 460 kN) and experienced a greater degree of deformation, including a greater ultimate displacement and a greater torsional angle at failure.

(2) Both the damaged and undamaged ends failed in a “bond-shear” mode, which is consistent with the theoretical models for girders with a small shear span-to-depth ratio. However, compared with those on the undamaged side, the pre-existing cracks on the T-A side intensified the failure process, leading to a much wider and more severe final crack state.

(3) A comparison of the experimental results with those of several calculation methods revealed varying levels of accuracy. Zhang's model and the ROSS model provided the most accurate predictions, with their ratios of experimental-to-predicted capacity closely matching 1.0. Naji's model proved to be the most

conservative, consistently yielding the largest safety margins. The AASHTO LRFD method, while conservative for the undamaged side (V_t/V_{pre} = 1.13), was slightly unconservative for the damaged side (V_t/V_{pre} = 0.94). This highlights a potential limitation of this code in accurately assessing the capacity of members with pre-existing damage.

In conclusion, this study confirms that pre-existing cracks resulting from operational damage can significantly compromise the shear capacity and overall structural stability of PC hollow core slabs. The findings underscore the importance of using refined analytical models, such as Zhang's model, for a more accurate assessment of damaged members, thereby providing a robust basis for informed maintenance and reconstruction strategies for aging bridge infrastructure.

Conflict of interest: All the authors disclosed no relevant relationships.

Data availability statement: The data that support the findings of this study are available from the corresponding author, Li, upon reasonable request.

Funding: This research was funded by Shanghai Municipal Transportation Commission Research Project (grant number is JT2024–KY–001). The authors extended their sincere gratitude for the support.

References

1. Jadwiga Osmolska, M.; Kanstad, T.; Hendriks, M.A.N.; Markeset, G. Numerical investigation into the effects of corrosion on the shear performance of pretensioned bridge girders with cast-in-place slabs. *Structures* **2022**, *46*, 1447-1468, doi:10.1016/j.istruc.2022.10.129.
2. Kotynia, R.; Przygocka, M. Preloading Effect on Strengthening Efficiency of RC Beams Strengthened with Non- and Pretensioned NSM Strips. *Polymers* **2018**, *10*, doi:10.3390/polym10020145.
3. Ross, B.E.; Hamilton, H.R.; Potter, W. Effect of Bearing Pad Arrangement on Capacity of Slab Panel Bridge Members. *Transportation Research Record: Journal of the Transportation Research Board* **2012**, *2313*, 92-99, doi:10.3141/2313-10.
4. Deatherage, J.H.; Burdette, E.G. Development Length and Lateral Spacing Requirements of Prestressing Strand for Prestressed Concrete Bridge Girders. *PCI Journal* **1994**, *39*, 70-83, doi:10.15554/pcij.01011994.70.83.
5. Zhang, F.; Zhao, G.-H.; Wu, Y.-F.; Zhang, Y. Effect of strand debonding on the shear strength of existing pretensioned PC hollow slab. *Engineering Structures* **2023**, *291*, doi:10.1016/j.engstruct.2023.116417.
6. Zhang, Y.; Huang, S.; Zhu, Y.; Hussein, H.H.; Shao, X. Experimental validation of damaged reinforced concrete beam strengthened by pretensioned prestressed ultra-high-performance concrete layer. *Engineering Structures* **2022**, *260*, doi:10.1016/j.engstruct.2022.114251.
7. Tadros, M.K.; Badie, S.S.; Tuan, C.Y. *Evaluation and Repair Procedures for Precast/Prestressed Concrete Girders with Longitudinal Cracking in the Web*; 2010.
8. Naji, B.; Ross, B.E.; W. Floyd, R. Characterization of Bond-Loss Failures in Pretensioned Concrete Girders. *J Bridge Eng* **2017**, *22*, doi:10.1061/(asce)be.1943-5592.0001025.
9. Ross, B.E.; Hamilton, H.R.; Consolazio, G.R. Experimental Study of End Region Detailing and Shear Behavior of Concrete I-Girders. *J Bridge Eng* **2015**, *20*, doi:10.1061/(asce)be.1943-5592.0000676.
10. Naji, B.; Ross, B.E.; Khademi, A. Analysis of Bond-Loss Resistance Models for Pretensioned I-Girders. *PCI Journal* **2018**, *63*, doi:10.15554/pcij63.1-03.
11. Murray, C.D.; Cranor, B.N.; Floyd, R.W.; Pei, J.-S. Experimental Testing of Older AASHTO Type II Bridge Girders with Corrosion Damage at the Ends. *PCI Journal* **2019**, *64*, doi:10.15554/pcij64.1-02.
12. Ross, B.E.; Ansley, M.H.; Hamilton, H.R. Load testing of 30-year-old AASHTO Type III highway bridge girders. *PCI Journal* **2011**, *56*, 152-163, doi:10.15554/pcij.09012011.152.163.
13. Tawadrous, R.; Morcous, G. Shear Strength of Deep Hollow-Core Slabs. *Aci Struct J* **2018**, *115*, doi:10.14359/51701298.
14. Ministry of Transport of the People's Republic of China JTG 3362—2018 Specifications for Design of Highway Reinforced Concrete and Prestressed Concrete Bridges and Culverts. China Communications Press: Beijing, 2018.

15. American Association of State Highway and Transportation Officials. AASHTO LRFD Bridge design specifications. Washington, DC, 2020.
16. Ross, B.E.; Naji, B. Model for Nominal Bond-Shear Capacity of Pretensioned Concrete Girders. *Transportation Research Record: Journal of the Transportation Research Board* **2014**, *2406*, 79-86, doi:10.3141/2406-09.
17. Hadrian software works. HADRIAN SOFTWARE WORKS n.d. Available online: (accessed on August 3, 2025).

AUTHOR BIOGRAPHIES

Jie Li
M.E., Engineer. Graduated from Tongji University in 2013. Working at Shanghai Municipal Road Transport Development Center.
Research Direction：Bridge Maintenance.
Email: 553766202@qq.com